Journal of Solid State Chemistry 182 (2009) 3320–3329

Contents lists available at ScienceDirect

Journal of Solid State Chemistry

journal homepage: www.elsevier.com/locate/jssc

Structural characterization of C–S–H and C–A–S–H samples—Part II: Local environment investigated by spectroscopic analyses

Guillaume Renaudin [a,d,*], Julie Russias [b], Fabrice Leroux [c,d], Céline Cau-dit-Coumes [b], Fabien Frizon [b]

[a] Clermont-Université, Ecole Nationale Supérieure de Chimie de Clermont-Ferrand, LMI, BP 10448, F-63000 Clermont-Ferrand, France
[b] Commissariat à l'Energie Atomique, DEN, Marcoule, Waste Treatment and Conditioning Research Department, F-30207 Bagnols sur Cèze, France
[c] Clermont Université, UBP, Laboratoire des Matériaux Inorganiques, F-63000 Clermont-Ferrand, France
[d] CNRS, UMR 6002, F-63177 Aubière Cedex, France

ARTICLE INFO

Article history:
Received 19 May 2009
Received in revised form
16 September 2009
Accepted 20 September 2009
Available online 2 October 2009

Keywords:
C–S–H
C–A–S–H
Tobermorite
^{27}Al NMR
^{23}Na NMR
^{1}H NMR
Raman spectroscopy

ABSTRACT

Spectroscopic studies (^{1}H, ^{23}Na and ^{27}Al MAS NMR and Raman spectroscopy) have been used to characterize three series of C–S–H samples ($0.8 < Ca/Si < 1.7$): one C–S–H series, one aluminum inserted C–S–H series (named C–A–S–H series), and one sodium and aluminum inserted C–S–H series (named C–N–A–S–H series). Previous Rietveld analyses have been performed on the two first series and have clearly shown that (1) a unique 'tobermorite M defect' structural model allows to describe the C–S–H structure whatever the Ca/Si ratio and (2) the insertion of aluminum into the C–S–H structure led to the degradation of the crystallinity and to a systematic increase of the basal spacing of about 2 Å regardless the Ca/(Si+Al) ratio (at a constant Al/Si ratio of 0.1). Spectroscopic investigations indicate that the main part of the Al atoms is readily incorporated into the interlayer region of the C–S–H structure. Al atoms are mainly inserted as four-fold coordinated aluminates in the dreierketten silicate chain (either in bridging or paired tetrahedra) at low Ca/Si ratio. Four-fold aluminates are progressively replaced by six-fold coordinated aluminates located into the interlayer region of the C–S–H structure and bonded to silicate chains. Investigation of the hydrogen bonding in C–S–H indicates that the main part of the hydrogen bonds is intra-main layer, and thus explains the low stacking cohesion of the C–S–H structure leading to its nanometric crystal size and the OD character of the tobermorite like structures.

1. Introduction

The insertion of Al atom in the C–S–H (calcium silicate hydrate) phase, the main component of Portland cement hydrated paste responsible for cohesion properties and durability, has been extensively studied [1–7]. Due to the lack of long-range ordering, NMR spectroscopy has been employed to characterize C–A–S–H phase (i.e. the Al inserted C–S–H phase) [8]. Indeed solid state ^{29}Si NMR studies have been performed to investigate the tobermorite-like structure of C–S–H (with a Ca/Si ratio varying between 0.6 and 2.0 for synthetic samples and a Ca/Si ratio close to 1.7 for Portland cement pastes [9–14]) which includes layers of seven-fold coordinated Ca^{2+} ions sandwiched in-between dreierketten chains of silicate tetrahedra (three-unit silicate tetrahedra) [12–20]. Results confirm the tobermorite-like structure of C–S–H with the observation of resonance lines coming from silicate end-groups (Si[Q^1]: $\delta \approx -79.5$ ppm) and from silicate tetrahedra taking part in chains as pure Q^2 units (Si[Q^2_P]: $\delta \approx -85.9$ ppm for the paired tetrahedra, and Si[Q^2_B]: $\delta \approx -82.6$ ppm for the bridging tetrahedra). At low Ca/Si ratio, a Si[Q^3]: $\delta \approx -92.5$ ppm has been observed and attributed to linking across the interlayer space of two silicate chains of two adjacent layers, which represents a defect in comparison with the tobermorite structure. An increase in the Ca/Si ratio results in the disappearance of Q^3, decreasing proportion of Q^2 and increasing proportion of Q^1 up to the complete elimination of the bridging silicon site, leading to a silicate structure only composed of dimers. ^{27}Al NMR spectroscopy has also been widely used to investigate the Al insertion into C–S–H phase [8,18–24]. Related ^{27}Al NMR spectra may exhibit diverse resonances from Al in IV-, V- and VI-fold oxygen coordination. Three Al[IV] signals are assigned to three types of aluminum incorporation in the tetrahedra of the dreierketten silicate chain: an Al[Q^3] bridging site ($\delta \approx 61$ ppm) across the interlayer [22] or between two dreierketten chains adjacent to the same main calcium oxide plan [24], an Al[Q^2_B] bridging site charge-balanced by interlayer Ca^{2+} ($\delta \approx 67$ ppm) and a third signal for $\delta \approx 72$ ppm. The latter resonance was first assigned to an Al[Q^2_B] bridging site charge-balanced by an interlayer or a surface Al[V]

* Corresponding author at: Clermont Université, Ecole Nationale Supérieure de Chimie de Clermont-Ferrand, LMI, BP 10448, F-63000 Clermont-Ferrand, France. Fax: +33 473 40 71 08.
E-mail address: guillaume.renaudin@ensccf.fr (G. Renaudin).

0022-4596/$ - see front matter © 2009 Elsevier Inc. All rights reserved.
doi:10.1016/j.jssc.2009.09.024

and/or Al[VI] [22], and was then attributed to an Al[Q_P^2] paired site [24]. Significant evidences were obtained (1) to locate the Al[V] site (resonance at $\delta \approx 39.9$ ppm) in the interlayer region of the C–S–H structure, potentially as Al^{3+} ions substituting for interlayer Ca^{2+} ions, and (2) to indicate that aluminum does not enter the Ca^{2+} main layer sites. Three Al[VI] resonances have been encountered and described in hydrated Portland cements: $\delta \approx 13$ ppm for ettringite, $\delta \approx 11$ ppm for AFm phases and $\delta \approx 5$ ppm related to C–A–S–H formation. The latter resonance, previously assigned to Al[VI] insertion in the interlayer space of C–S–H [22], has been recently assigned to an amorphous aluminate hydrate associated with the C–A–S–H precipitation [23].

In the first part of the present study [25], Rietveld refinements performed on C–S–H and C–A–S–H series ($0.8 < Ca/Si < 1.7$) have shown the systematic worsening of the crystallinity and a systematic layer spacing increase of about 2 Å when aluminum is inserted in C–S–H whatever the Ca/Si ratio between 0.8 and 1.7 (as already mentioned in the literature [22,24]). The aluminum insertion in the silicate tetrahedra (Al[IV] signals of the ^{27}Al NMR spectra) or in the interlayer calcium site (Al[V] and/or Al[VI] signals of the ^{27}Al NMR spectra) as reported in the literature did not allow to explain such a large increase in the interlayer space. This prompts us to investigate here more precisely the aluminum incorporation into the C–S–H structure (i.e. the highly disordered interlayer region of C–A–S–H) by rationalizing the data obtained from a combination of techniques (^{1}H, ^{23}Na, ^{27}Al NMR and Raman spectroscopy) over the different substitution domains.

2. Experimental

2.1. CSH and CASH syntheses

Syntheses of C–S–H and Na-free C–A–S–H samples are described in the first part of the study [25]. The samples studied have been designed by C–S–H_*n* and C–A–S–H_*n*, with *n*=0.8, 1.0, 1.1, 1.3, 1.5 and 1.7 for, respectively, the Al-free and Al-containing series.

A third series of samples, Na containing C–A–S–H with $0.8 < Ca/Si < 1.7$, have been synthesized in order to examine the correlations between the ^{23}Na NMR signals and the ^{27}Al NMR signals. These Na-containing samples have been labeled C–N–A–S–H_*n* with *n*=0.8, 1.0, 1.1, 1.5 and 1.7. Samples from the C–N–A–S–H series were synthesized from silica (Degussa, Aerosil 380), calcium oxide (Aldrich, 99.9% pure) freshly decarbonated 3 h at 900 °C and sodium aluminate $NaAlO_2$ (Sigma-Aldrich, $\leq 0.05\%$ total Fe impurities) following the protocol described in [23]. Demineralized and decarbonated water were added to reach a water/solid ratio of 50 and the Al/Si and Na/Si molar ratios were adjusted to 0.1. All the syntheses were stored at 20 °C under N_2 atmosphere for three weeks under stirring in closed polypropylene bottles. They were then filtered under nitrogen and rinsed with acetone. The precipitates were subsequently dried in a desiccator, under slight vacuum, over silica gel, at room temperature. Experimental conditions are summarized in Table 1. The chemical analyses of the filtered solutions in equilibrium with the solid phases show that the amount of sodium incorporated in C–N–A–S–H samples decreases with increasing alumina+silica content.

Table 1
Starting material amounts for the different syntheses.

	Nominal composition: Ca/Si ratio				
	0.8	1.0	1.1	1.5	1.7
C–N–A–S–H					
CaO (mmol)	39.64	44.85	47.10	54.37	57.25
SiO_2 (mmol)	45.04	40.78	38.93	32.95	30.61
$NaAlO_2$ (mmol)	4.55	4.15	3.97	3.40	3.17
Water (mL)	265	265	265	265	265
Experimental Ca/(Al+Si) ratio[a]	0.76	0.91	0.99	1.26	1.44
Experimental Ca/Si ratio[a]	0.84	1.00	1.09	1.39	1.58
Experimental Na/Al[a]	0.56	0.30	0.24	0.08	0.08

[a] Calculated from ICP-MS analyses of the filtered solutions after the three weeks of synthesis in polypropylene bottle.

2.2. Analytical techniques

2.2.1. ^{1}H, ^{23}Na and ^{27}Al MAS NMR spectroscopies

High resolution ^{1}H, ^{23}Na, and ^{27}Al MAS NMR spectra were collected on a Bruker 300 instrument operating at 7.04 T, the Larmor frequencies being, respectively, equal to 300, 79.39 and 78.20 MHz. 4 mm-diameter zirconia rotors were spinned at 10 kHz during the MAS conditions, therefore the central transition $(+\frac{1}{2}, -\frac{1}{2})$ was recorded only.

Single pulse experiment was applied for the three nuclei, and the parameters were optimized for each nucleus. However, the quadrupolar nature of the ^{23}Na (3/2) and ^{27}Al (5/2) nuclei required that the flip angle should satisfy the condition $(I+\frac{1}{2}) \cdot \omega_{RF} \cdot t_p \leq \pi/6$ where ω_{RF} (rad s^{-1}) is the Larmor frequency of the corresponding quadrupolar nuclei and t_p (s) the pulse time. Small pulse angle of about 10° corresponding to 0.8–1.2 ms pulses were used in the MAS sequence. This was associated to a recycling time of 2 s. Calibration was adjusted with the resonance line of adamantane at 1.7 ppm, NaCl at 0 ppm, and $AlCl_3$ at 0 ppm for ^{1}H, ^{23}Na, and ^{27}Al, respectively. A collection of 10, 500, and 2000 transients to get a proper signal to noise response was necessary for ^{1}H, ^{23}Na, and ^{27}Al nuclei, respectively. Single pulse experiment is quantitative and therefore the relative nuclei site population was accessible. However, for noninteger quadrupolar nuclei, the central transition is not perturbed by the first order quadrupolar interaction, while the second order is known to broaden the resonance line as well as to shift its position from the isotropic chemical shift. The fast MAS spectrum of the central $(+\frac{1}{2}, -\frac{1}{2})$ is then shifted from the center of gravity by the second order quadrupolar interaction

$$\delta^{(2)}_{QS(+1/2,-1/2)} = -\frac{3C_Q^2}{40\omega_0^2} \cdot \left[\frac{I(I+1) - 3/4}{I^2(2I-1)^2}\right] \cdot \left(1 + \frac{\eta^2}{3}\right)$$

where C_Q is the quadrupolar coupling ($C_Q = e^2 \cdot q \cdot Q/h$, where $e \cdot q$ is the electric field gradient and $e \cdot Q$ is the quadrupolar moment of values of 0.1×10^{28} Q/m^2 for ^{23}Na nuclei and 0.15×10^{28} Q/m^2 for ^{27}Al nuclei), and η the asymmetry parameter. The isotropic chemical shift position and the quadrupolar frequency ν_Q (responsible for $\delta^{(2)}_{QS(+1/2,-1/2)}$) may be obtained by measurements either at different magnetic fields [23] or of the central and of the sideband patterns of the satellite transitions [26]. The shift of the central band is then given by

$$\delta^{(2)}_{QS(+1/2,-1)} = -\frac{\nu_Q^2}{30\nu_0^2}[I(I+1) - 3/4] \times 10^6$$

which can be further calculated for ^{23}Na and ^{27}Al by

$$\delta^{(2)}_{QS(+1/2,-1/2)} = -\frac{\nu_Q^2}{10\nu_0^2} \times 10^6$$

and

$$\delta^{(2)}_{QS(+1/2,-1/2)} = -\frac{8\nu_Q^2}{30\nu_0^2} \times 10^6,$$

respectively. For ^{27}Al, ν_Q ranges from 0.15 to 0.35 for Al(VI), from 0.4 to 0.5 for Al(V) and from 0.2 to 0.5 for Al(IV) [21,22].

In the following the chemical shifts are neither corrected for second-order quadrupolar effects nor reported as isotropic values. Indeed the maximum intensity positions are comparatively discussed for the series.

2.2.2. Raman spectroscopy

Micro-Raman spectra were recorded at room temperature in the back scattering geometry, using a Jobin-Yvon T64000 device. The spectral resolution obtained with an excitation source at 514.5 nm (argon ion laser line, Spectra Physics 2017) is about 1 cm^{-1}. The Raman detector was a charge coupled device (CCD) multichannel detector cooled by liquid nitrogen to 140 K. The laser beam was focused onto the sample through an Olympus confocal microscope with $\times 100$ magnification. Laser spot was about 1 μm^2. Measured power at the sample level was kept low (<10 mW) in order to avoid any damage of the material. The Raman scattered light was collected with the microscope objective at 180° from the excitation and filtered with an holographic Notch filter before being dispersed by a single grating (1800 grooves per nm). Spectra were recorded (four scans of 300 s each) in the frequency ranges 300–1400 cm^{-1} and 3100–3900 cm^{-1} in order to investigate, respectively, the Raman active vibration modes of silicate tetrahedra (Si[Q^n]) and the hydrogen bond network due to O–H stretching. Spectra were analyzed by a profile fitting procedure using a Lorentzian function.

3. Results

3.1. ^{27}Al MAS NMR spectroscopy

The C–A–S–H series: ^{27}Al MAS NMR spectra recorded on the series of the aluminum incorporated C–S–H samples (see Fig. 1a) show the three IV-, V- and VI-coordination for Al (Al[IV], Al[V] and Al[VI]) in agreement with the literature [21,22,24]. The resolution of the spectra allows us to observe and decompose five distinct signals: two assignable to Al[IV] (with peak maxima near 60 and 69 ppm, designed, respectively, by δ_{Al1} and δ_{Al2} in the text), one Al[V] (with peak maximum near 33 ppm, designed by δ_{Al3}) and two Al[VI] (with peak maxima near 3.5 and 9.5 ppm, designed, respectively, by δ_{Al4} and δ_{Al5}). Al[IV] signal near 60 ppm (δ_{Al1}) is attributed to an Al[Q^3] bridging site [22,24]. Two other Al[IV] signals are reported in the literature: one near 67 ppm attributed to an Al[Q^2_B] bridging site charge-balanced by interlayer Ca^{2+} and one near 72 ppm attributed to an Al[Q^2_B] bridging site charge-balanced by interlayer Al[V] and Al[VI] by Sun et al. [22] or attributed to an Al[Q^2_P] paired site by Chen [24]. The resolution of our NMR spectra did not allow decomposing these two contributions. One broad signal with a mean maximum near 69 ppm (δ_{Al2}) was considered only. The broad Al[IV] line shape can be explained by a distribution of electric field gradients coming from a large degree of structural disorder. δ_{Al2} presents a marked asymmetry in its MAS line shape with a broadening more pronounced on the shielded side. The broad down-shielded Al[IV] line shapes can be explained by a higher quadrupolar distribution, thus lowering the resolution of the tetrahedral contribution and making the site assignments difficult [27]. Nevertheless a shift toward the high isotropic chemical shifts was observed when increasing the Ca/Si ratio: from 68 ppm for C–A–S–H_0.8 to 70 ppm for C–A–S–H_1.7. This down-field shift of the δ_{Al2} signal agrees well with an aluminum substitution in paired tetrahedra for high Ca/Si values. When increasing the Ca/Si ratio, i.e. decreasing the dreierketten silicate polymerization, the amount of bridging sites decreases and inversely the paired sites should increase. This corresponds alternatively to a decrease for both Al[Q^3] and Al[Q^2_B] signals and an increase in Al[Q^2_P] signal. Fig. 2 shows the population (normalized at 100%) of the three aluminum coordinations: Al[IV] (sum of the two δ_{Al1} and δ_{Al2} signals), Al[V] (δ_{Al3} signal) and Al[VI] (sum of the two δ_{Al4} and δ_{Al5} signals) versus the Ca/Si ratio. Results of the profile fitting analysis are gathered in Table 2. The changes in the IV- and VI-coordination populations are linearly dependant on the Ca/Si ratio. When increasing the Ca/Si value, tetrahedral coordination of aluminum (Al[IV] is predominant with more than 70% in C–A–S–H_0.8) is gradually replaced by octahedral coordination of aluminum (Al[VI] becomes preponderant with more than 70% in C–A–S–H_1.7). The population assigned to the pentahedral coordinated Al[V] is almost constant, close to 10% whatever the Ca/Si value. The assignment for δ_{Al1} and δ_{Al2} is somehow consistent with what should be expected from the population change against the Ca/Si ratio. Indeed a continuous decrease of Al[Q^3], i.e. δ_{Al1} resonance line, when Ca/Si increases pictures well

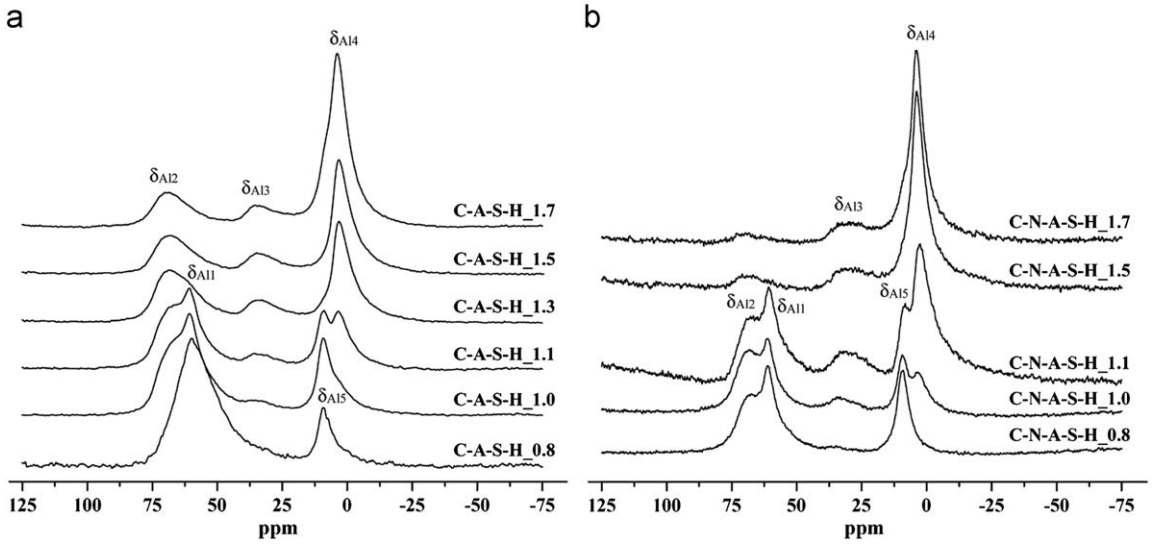

Fig. 1. ^{27}Al MAS NMR spectra from samples belonging to (a) the C–A–S–H series and (b) the C–N–A–S–H series. Spectra are composed of five distinct resonance contributions labeled δ_{Al1} and δ_{Al2} (two IV-coordinated aluminum), δ_{Al3} (one V-coordinated aluminum), δ_{Al4} and δ_{Al5} (two VI-coordinated aluminum).

the dreierketten silicate chain polymerization decrease. Al[Q^2_B] and Al[Q^2_P] sites are here not distinguished making difficult the tendency, however, the whole Al[IV] population decreases to the profit of Al[VI]. The population of δ_{Al2} signal increases strongly when the Ca/Si ratio is changed from 0.8 to 1.0 only: from 5% in C–A–S–H_0.8 to 20% in C–A–S–H_1.0 (this corresponds to the replacement of the decreasing Al[Q^3] bridging site by Al[Q^2_B] bridging site). After that, it is quite constant, or slightly decreasing down to 10% in C–A–S–H_1.7 (this corresponds to the gradual replacement of Al[Q^2_B] bridging site by Al[Q^2_P] paired site when decreasing the dreierketten silicate chain polymerization). The evolution of both δ_{Al4} and δ_{Al5} lines gives clear evidence for the direct incorporation of the VI-coordinated aluminum atoms into C–A–S–H. The basal spacing of about 2 Å greater for the C–A–S–H series than for the C–S–H series whatever the Ca/Si ratio indicates that aluminum cations are readily incorporated into C–A–S–H [25]. Concerning the presence of impurity, the monocarboaluminate phase has been observed in C–A–S–H_1.7 only (i.e. the carbonated AFm phase [28,29] with a refined weight amount about 5 wt% [25]). The large majority of Al[VI] observed in samples C–A–S–H_1.5 and C–A–S–H_1.7 cannot be explained by the presence of the AFm phase only. The isotropic chemical shift near 9 ppm (line δ_{Al5}), generally attributed to the presence of AFm phase [20,23,24] (an isotropic chemical shift at 10.2 ppm has been determined for the monosulfoaluminate phase [30]) is weak in intensity in our samples and decreases when Ca/Si ratio increases (from 13% in C–A–S–H_0.8 to 0% in C–A–S–H_1.5). The main part of the VI-coordinated aluminum atoms shows an isotropic chemical shift near 3.5 ppm (narrow line), and the corresponding population largely increases as the Ca/Si ratio increases (from 5% in C–A–S–H_0.8 to about 70% in C–A–S–H_1.7). This signal is already significant for C–A–S–H_1.0 and C–A–S–H_1.1 (respectively, 18% and 28%) and becomes majority from C–A–S–H_1.3 (58% for C–A–S–H_1.5 and 65% for C–A–S–H_1.7). An isotropic chemical shift close to 5 ppm has been assigned to an amorphous aluminate hydrate precipitated at the surface of the C–S–H phase [23]. Gibbsite shows two octahedral ^{27}Al NMR components: a main signal at 8 ppm and a weak signal at 1 ppm [31]. Our results give evidence for the location of an Al[VI] site, with an isotropic chemical shift near 3 ppm, which is actually located into the interlayer region of the C–A–S–H phase in order to explain the basal spacing increase of about 2 Å observed by XRD when incorporating aluminum [25]. These inserted Al[VI] species should be connected to the interlayer calcium cations in order to form an AFm-type calcium aluminate layer. This assumes specific crystallographic sites for the VI-coordinated aluminum atoms into the interlayer region of the C–A–S–H structure and correlates the structural observations made in the first part of this study [25]: (1) Al atoms are not simply substituted to Si atoms, and (2) tobermorite M model cannot describe accurately the structure of C–A–S–H samples, especially at high Ca/Si ratio (due to the discrepancy between the refined and the nominal Ca/Si ratios; see Fig. 5 from Renaudin et al. [25]).

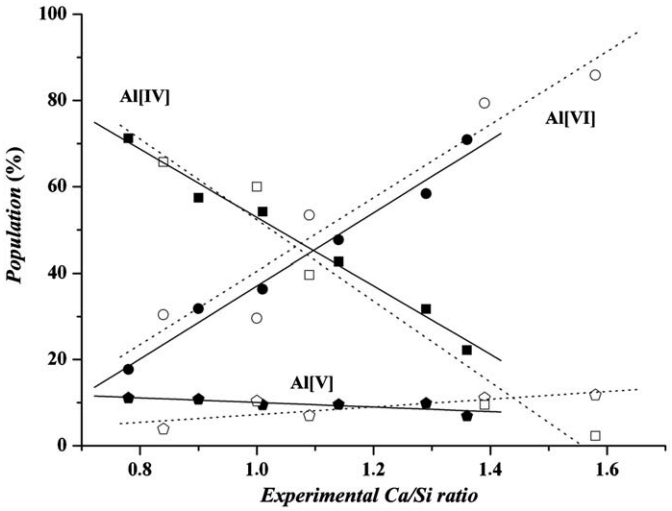

Fig. 2. Populations of the IV-, V- and VI-coordinated aluminum atoms (Al[IV], Al[V] and Al[VI] represented, respectively, by squares, pentagons and circles) inserted in the C–S–H structure obtained from the profile fitting analyses of the ^{27}MAS NMR spectra from samples belonging the C–A–S–H series (filled symbols and full lines) and from samples belonging the C–N–A–S–H series (opened symbol and dotted lines).

The C–N–A–S–H series: ^{27}Al MAS NMR spectra of the Na containing C–A–S–H samples (i.e. the C–N–A–S–H samples) are shown in Fig. 1b. Results of the profile fitting procedure by using five distinct signals are reported in Table 2 and Fig. 2. Observations are equivalent with those from the C–A–S–H series: gradual replacement of Al[IV] by Al[VI] as the Ca/Si ratio increases, and a quite constant amount of Al[V] close to 10% (or weakly increasing with the Ca/Si ratio). The presence of sodium cations into the interlayer region of the C–S–H structure did not perturb, or modify, the aluminum intercalation. When increasing the Ca/Si ratio in the C–N–A–S–H series the dreierketten silicate chain polymerization is decreasing and IV-coordinated aluminum atoms are destabilized to the profit of VI-coordinated aluminum atoms from the previously described AFm-type layer.

Table 2
Results of the profile fitting analyses using five components (δ_{Al1}–δ_{Al5}) of the ^{27}Al MAS NMR spectra from the C–A–S–H and the C–N–A–S–H series.

Samples	Al[IV]				Al[V]		Al[VI]			
	δ_{Al1} (ppm)	Pop. (%)[a]	δ_{Al2} (ppm)	Pop. (%)[a]	δ_{Al3} (ppm)	Pop. (%)[a]	δ_{Al4} (ppm)	Pop. (%)[a]	δ_{Al5} (ppm)	Pop. (%)[a]
C–A–S–H_0.8	59.9	66	68	5	34.2	11	3.5	5	9.1	13
C–A–S–H_1.0	60.5	37	68.5	20	33.9	11	3.7	18	9.2	14
C–A–S–H_1.1	60.8	37	69.9	17	33.8	9	3.0	28	9.6	9
C–A–S–H_1.3	61.1	29	69.8	15	32.7	10	3.2	45	9.2	3
C–A–S–H_1.5	59.2	16	69.4	16	32.9	10	3.3	58	9.0	0
C–A–S–H_1.7	61.8	12	70.1	10	33.5	7	3.6	65	9.3	6
C–N–A–S–H_0.8	61.0	43	69.6	23	35.3	4	–	0	9.2	30
C–N–A–S–H_1.0	61.0	29	69.4	31	33.1	10	2.9	17	9.3	13
C–N–A–S–H_1.1	60.5	24	69.0	15	30.5	7	2.1	51	9.1	3
C–N–A–S–H_1.5	–	0	68.8	10	29.7	11	3.3	78	9.4	1
C–N–A–S–H_1.7	–	0	69.7	2	29.6	12	3.7	85	9.7	1

[a] Relative populations of the five signals obtained by profile fitting of the ^{27}Al NMR spectra (normalized at 100% of aluminum atoms).

3.2. ^{23}Na MAS NMR spectroscopy

The general ^{23}Na MAS spectra shape is rather similar to the freeze-dried samples obtained from the interaction of NaCl with C–S–H [1]. However, in contrast to Viallis et al. [32], where no difference between the two Na resonance intensities was noticed regardless of the Ca/Si ratio, a pronounced change of population is here observed. Two components are distinguished in the ^{23}Na MAS NMR spectra from the C–N–A–S–H series (see Fig. 3a): one sharp signal at −7.6 ppm (δ_{Na1}) and one large signal centered near −10 ppm (δ_{Na2}). The large predominant δ_{Na2} signal in C–N–A–S–H_0.8 sample can be compared to the Na2 site designed by Viallis et al. [32] around −13 ppm attributed to Na^+ aqueous outer complex (the broadening of the line may be attributed to a distribution of the adsorption surface sites). When increasing the Ca/Si ratio the sharp δ_{Na1} signal becomes more and more intense (until forming the main response for C–N–A–S–H_1.5 and C–N–A–S–H_1.7 samples).

The sharp δ_{Na1} resonance line for the ^{23}Na central transition is characteristic of either perfect point symmetry (i.e. a high symmetry Na site) or a highly mobile Na^+ ion, since both effects will result in no quadrupolar interaction. It is important to note that a small site distortion should also give rise to unperturbed central transition. It is known that Na^+ is usually fully hydrated (outer-sphere complexes) and that Na^+ forms a diffuse ion swarm (not localized) [32,33]. The present used NMR sequence cannot distinguish outer-sphere Na cations from diffuse layer, the dynamic exchange being rather high in both cases [32,33]. However, an assignment of highly symmetrical site for δ_{Na1} is here rather favored due to the low water content of our samples and due to the low ionic mobility (determined by complex impedance spectroscopy measurements not shown here). The evolution of δ_{Na1} signal seems strongly correlated to δ_{Al4} (i.e. the VI-coordinated aluminum inserted in the interlayer region of C–S–H) as represented in Fig. 3b. For higher Ca/Si ratio, C–S–H phase incorporates interlayer octahedral aluminates imbalanced by interlayer Na^+ cations. The observed δ_{Na1} isotropic chemical shift is somehow comparable to the ^{23}Na MAS NMR signal for the silico-aluminate compound $NaAlSi_3O_8$ (−8.5 ppm [34]) having an average Na-O distance of about 2.7 Å.

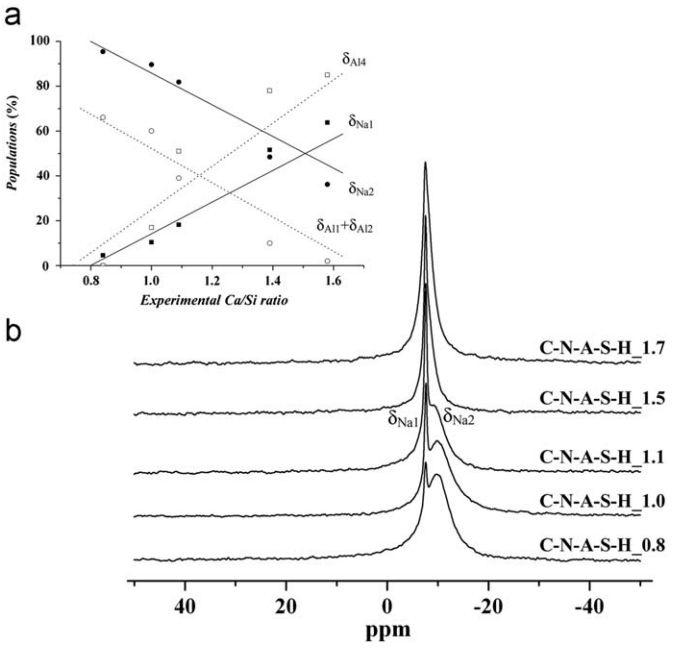

Fig. 3. ^{23}Na MAS NMR spectra from samples belonging to the C–N–A–S–H series (a) and results of the profile fitting of two components δ_{Na1} and δ_{Na2} (normalized at 100% of sodium atoms) superimposed with the $\delta_{Al1}+\delta_{Al2}$ (Al[IV]) and δ_{Al4} (Al[VI]) populations) (b) linear fitting are just guides for the eyes).

Concerning the ill defined high-field shifted line δ_{Na2}, the spinning speed is not fast enough for the line narrowing. Such a line broadening may result from the combination of hetero-dipolar and quadrupolar interactions, and chemical shift anisotropy. Indeed the quadrupolar moment of ^{23}Na is relatively of small amplitude (experimental section), and the line broadening may be rather attributed to either an inhomogeneous distribution of sites with comparable low mobility or a rigid low symmetrical environment for the Na^+ cations (unexchangeable cation). Additionally δ_{Na2} site population seems to correlate the IV-coordinated aluminum atoms ($\delta_{Al1}+\delta_{Al2}$, see Fig. 3b). This may indicate a restricted motion of Na^+ present in the interlayer region of the rigid crystalline framework, in the vicinity of Al[IV]. The more shielded values for δ_{Na2} suggest that its neighboring coordination (and associated electronegativity) is slightly higher than for the δ_{Na1} local environment [33].

Then, it seems reasonable to surmise that sharp δ_{Na1} signal is related to high symmetrical Na^+ cation rigidly held in the structure correlated to Al[VI], whereas broad δ_{Na2} signal is related to low symmetrical Na^+ cation rigidly held in the structure correlated to Al[IV]. Nevertheless the contribution of mobile adsorbed Na^+ cation could not be excluded (either at the C–A–S–H particles surface or within the interlayer region of C–A–S–H).

3.3. Raman spectroscopy

Raman spectroscopy has been used to investigate the silicate tetrahedra connectivity for the C–S–H, the C–A–S–H and the C–N–A–S–H series. Raman spectra from samples belonging to the C–N–A–S–H series are similar to those from the C–A–S–H series. Spectra from C–N–A–S–H series are not shown here. Profile fitting results from the three series are gathered in Table 3. Previous Raman spectroscopic analyses have been performed on C–S–H samples by Kirkpatrick et al. [35] and Garbev et al. [36,37]. The presence of distinct symmetrical Si–O stretching mode vibration for Si[Q^1], Si[Q^2] and Si[Q^3] allows the investigation of the silicate polymerization in the dreierketten silicate chain even in absence of a long-range structural order. Raman spectroscopy presents the strong advantage to have an experimental setup particularly convenient since no particular preparation of the sample is required and is less time-consuming than ^{29}Si NMR spectroscopy. In C–S–H compounds, the Si[Q^1], Si[Q^2] and Si[Q^3] environments show symmetric stretching modes of vibration, respectively, in the ranges 870–900, 950–1010 and around 1080 cm^{-1}.

Fig. 4a shows the Raman spectra in the range 300–1400 cm^{-1} recorded from samples belonging to the C–S–H series. Four vibrations are observed from these spectra: (1) a band near 680 cm^{-1} visible whatever the Ca/Si value and assigned to symmetric bending of the Si_P–O–Si_P linkage of Si[Q^2_P] paired tetrahedra, (2) a band near 890 cm^{-1} which appears in the C–S–H_1.0 sample and increases in intensity with the Ca/Si value, assigned to the symmetric stretching mode of the Si[Q^1] tetrahedra, (3) a band near 1010 cm^{-1} present in all spectra which decreases in intensity when the Ca/Si value increases, and assigned to the symmetric stretching mode of the Si[Q^2] tetrahedra, and finally (4) a band near 1080 cm^{-1} present in all spectra (the broad weak band observed in C–S–H_0.8 and C–S–H_1.0 becomes sharper with an increasing intensity when the Ca/Si ratio increases) assigned to Si[Q^3] tetrahedra. The symmetrical C–O stretching mode of carbonate group, ν_1 [CO_3], appears near 1080 cm^{-1}, in the region of the Si[Q^3] tetrahedral signal. Line profile

Table 3
Profile fitting results obtained from the Raman spectra of samples belonging to the C–S–H, C–A–S–H and C–N–A–S–H series.

Samples	Assignments									
	v_2 $[Q_P^2]$[a]		v_1 $[Q^1]$[b]		v_3 $[Q^1]$[c]		v_1 $[Q^2]$[b]		v_1 $[Q^3]$[b]/v_1 $[CO_3]$[d]	
	Raman shift (cm^{-1})	FWHM (cm^{-1})	Raman shift (cm^{-1})	FWHM (cm^{-1})	Raman shift (cm^{-1})	FWHM (cm^{-1})	Raman shift (cm^{-1})	FWHM (cm^{-1})	Raman shift (cm^{-1})	FWHM (cm^{-1})
C–S–H_0.8	670	24	–	–	–	–	1008	64	1079	59
C–S–H_1.0	674	38	874	87	–	–	1014	80	1078	24
C–S–H_1.1	675	39	884	73	981	60	1023	46	1081	26
C–S–H_1.3	677	38	881	56	983	41	1024	31	1081	26
C–S–H_1.5	678	38	886	53	981	48	1026	31	1082	22
C–S–H_1.7	675	37	884	59	977	55	1022	33	1080	28
C–A–S–H_0.8	672	40	–	–	–	–	1009	62	1078	29
C–A–S–H_1.0	679	42	–	–	–	–	1004	76	1075	26
C–A–S–H_1.1	675	34	–	–	–	–	999	69	1074	20
C–A–S–H_1.3	674	36	–	–	–	–	990	93	1077	27
C–A–S–H_1.5	674	37	891[w]	74	–	–	991	87	1076	22
C–A–S–H_1.7	673	33	893	76	–	–	991	78	1073	20
C–N–A–S–H_0.8	670	39	–	–	–	–	1005	73	1078	24
C–N–A–S–H_1.0	671	34	–	–	–	–	1001	71	1080	35
C–N–A–S–H_1.1	673	46	–	–	–	–	1000	77	1079	23
C–N–A–S–H_1.5	674	39	867[w]	44	–	–	999	55	1078	21
C–N–A–S–H_1.7	674	44	854[w]	47	–	–	995	51	1080	22

[a] Symmetric bending of the Si_P–O–Si_P linkage of Si$[Q_P^2]$ paired tetrahedra.
[b] Symmetric stretching of $[SiO_4]$ in Q^n linkage.
[c] Asymmetric stretching of $[SiO_4]$ in Q^1 linkage.
[d] Symmetric stretching of $[CO_3]$.
[w] Indicates band of vibration with weak intensity.

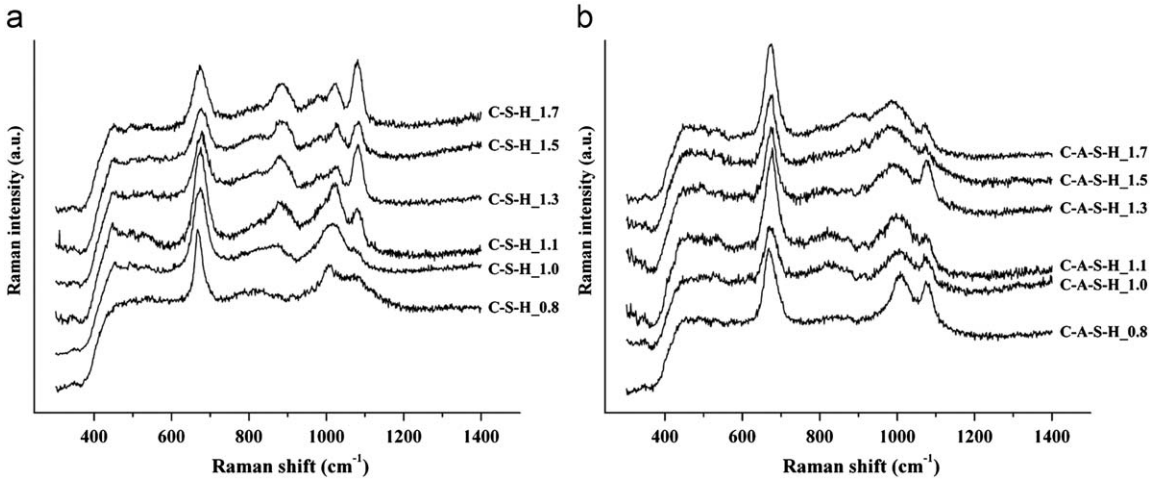

Fig. 4. Raman spectra in the range 400–1400 cm^{-1} of samples belonging to (a) the C–S–H series and (b) the C–A–S–H series (similar spectra were recorded from samples belonging to the C–N–A–S–H series).

fitting results are gathered in Table 3. Observations from the range 200–1300 cm^{-1} agree with the known decrease in polymerization degree of the dreierketten silicate chains when increasing the Ca/Si ratio. The increase in the intensity of the symmetric stretching Si$[Q^1]$ mode and decrease in the symmetric stretching Si$[Q^2]$ mode is indicative of the gradual transition from linear silicate chains (low Ca/Si ratio) to dimeric silicate tetrahedra (high Ca/Si ratio). The vibration observed at 1080 cm^{-1} should be attributed to two modes of vibration: the symmetric stretching Si$[Q^3]$ mode mainly observed for C–S–H_0.8 showing a broad band of vibration and disappearing for Ca/Si > 1.0, and a sharper band corresponding to the symmetrical C–O stretching mode of carbonate group, v_1 $[CO_3]$, which increases in intensity when the Ca/Si ratio increases (i.e. when the CaO amount increases). Due to the high scattering cross-section of the v_1 $[CO_3]$ mode, even a small carbonation (which has been previously detected by TGA-MS analyses [25]) of our samples yields to a relatively intense band observed in Raman spectra near 1080 cm^{-1}. A fifth weak band, attributed to the asymmetric stretching Si$[Q^1]$ mode, is observed near 980 cm^{-1} for samples from C–S–H_1.1 to C–S–H_1.7. The symmetric stretching Si$[Q^2]$ mode shifts toward the high Raman shifts when Ca/Si increases (from 1008 cm^{-1} for C–S–H_0.8 to about 1025 cm^{-1} for CSH_1.5 and C–S–H_1.7). This shift has to be explained by the progressive transformation of the infinite silicate chains (with one Si$[Q_B^2]$ bridging tetrahedron for two Si$[Q_P^2]$ paired tetrahedra showing an average Si$[Q^2]$ Raman

shift at about 1010 cm^{-1}) to dimeric silicate tetrahedra. The decrease in the degree of silicate polymerization leads to the formation of defined silicate species (as octamers or pentamers) and results in the observed Raman shift displacement and band sharpening.

Spectra recorded from samples belonging to the C–A–S–H and C–N–A–S–H series show a different evolution of their symmetric stretching Si[Q^n] modes (see Fig. 4b and Table 3). The symmetric stretching Si[Q^1] band is quite never observed and the symmetric stretching Si[Q^2] band has a quite constant intensity whatever the Ca/Si ratio. Evolution of the symmetric stretching Si[Q^3] band is hindered by the overlapped ν_1 [CO_3] band. Nevertheless samples from the C–A–S–H series seem to be less carbonated than those from the C–S–H series, namely for the high Ca/Si ratio. Raman spectroscopy clearly evidences the higher degree of silicate polymerization in the C–A–S–H series and also in the C–N–A–S–H series (compared to the C–S–H series) as already mentioned in the literature [6,18,22,23]. The evolution of the Si[Q^2] band in C–A–S–H and C–N–A–S–H series are opposite to the Si[Q^2] band evolution previously described for the C–S–H series (which increases from 1008 cm^{-1} for C–S–H_0.8 up to about 1025 cm^{-1} for C–S–H_1.5 and C–S–H_1.7). Not only the Si[Q^2] Raman shift is not increasing when Ca/Si ratio increases (due to the fact that the shortening of the silicate chains length was not observed when introducing aluminum atoms in the C–S–H structure), but it decreases down to about 990 cm^{-1} for C–A–S–H_1.7 sample and about 995 cm^{-1} for C–N–A–S–H_1.7 sample. The broadening and the shift toward the low Raman shifts of the symmetric stretching Si[Q^2] band is certainly due to: (1) the presence Al[IV] in the silicate chain in a first step, and (2) the presence of interlayer Al[V] and the progressive insertion of Al[VI] into the interlayer region of the C–S–H structure. Interlayer Al[V] and Al[VI] aluminates, connected to interlayer Ca^{2+} cations, should be directly connected to silicate chains in order to keep constant or increase the degree of silicate polymerization. The quite invariant Raman shift value for the symmetric bending of the Si_P–O–Si_P linkage of Si[Q^2_P] paired tetrahedra indicates that the Si_P–O–Si_P angle ranges always around 140°, [36] independently from the presence or absence of aluminum and independently from the Ca/Si ratio.

3.4. Investigation of the hydrogen bonds network

Raman spectroscopy: The Raman spectral range 3000–4000 cm^{-1} is a useful tool to investigate the hydrogen bond network in cement hydrates [38,39]. Fig. 5 shows the Raman spectra for samples belonging to the C–S–H series and C–A–S–H series. Unexpectedly all samples show similar spectra (in band positions as well as in intensity) whether Al is inserted or not and this over the entire domain of composition. Two groups of Raman active vibrations are observed: one band centered at 3227 ($\pm$1) cm^{-1} and one broader band centered at 3474 ($\pm$1) cm^{-1} with two shoulders close to 3454 ($\pm$3) cm^{-1} and 3489 ($\pm$3) cm^{-1}. C–S–H_1.5 and C–S–H_1.7 samples also show a sharp band at 3620 cm^{-1} corresponding to the A_{1g} (OH) mode from portlandite [40] (see stars in Fig. 5). The invariability in the 12 Raman spectra indicates clearly that all the synthesized C–S–H and C–A–S–H samples have exactly the same hydrogen bonds network. Therefore hydrogen bonding should be located in a

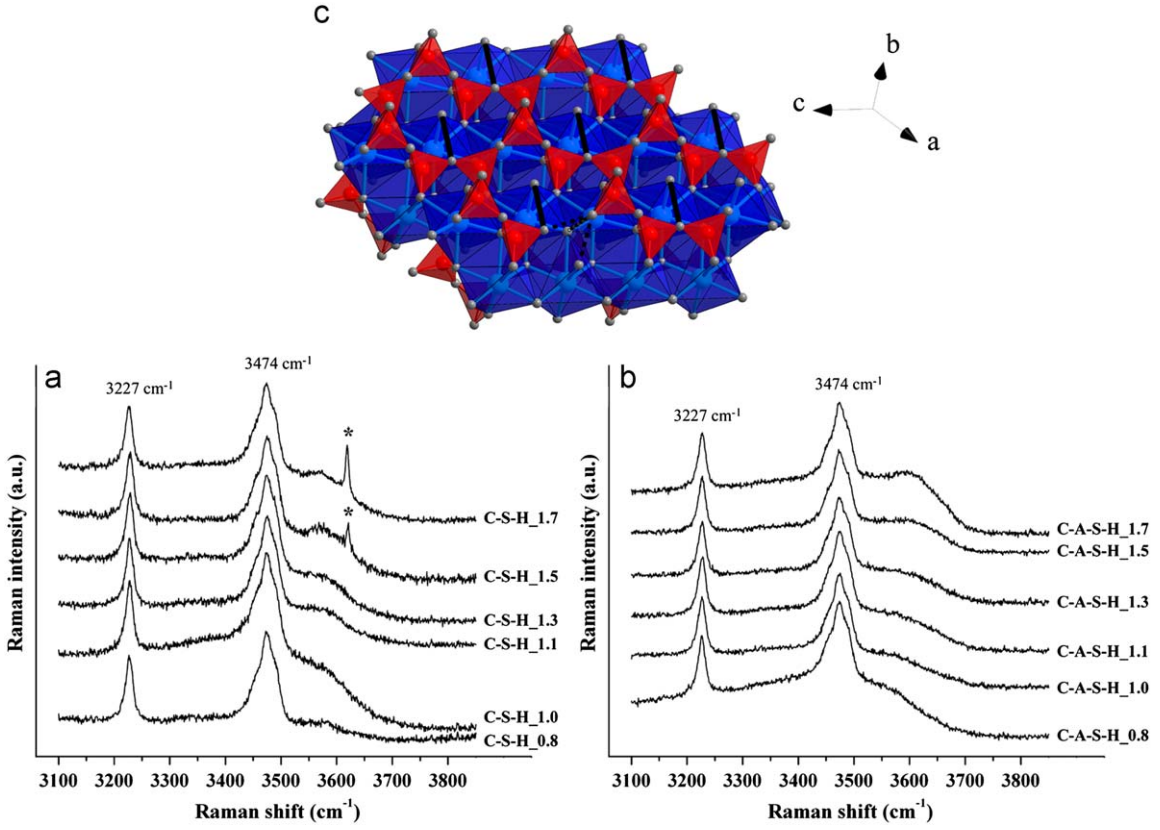

Fig. 5. Raman spectra in the range 3100–3900 cm^{-1} of samples belonging to (a) the C–S–H series and (b) the C–A–S–H series (similar spectra were recorded from samples belonging to the C–N–A–S–H series) showing the OH symmetric stretching (stars indicate vibration from portlandite). Identified hydrogen bonds are drawing (c) full black bonds for intra-main layer hydrogen bond, and dashed black bonds for possible hydrogen bond when missing one paired silicate tetrahedra (red and blue polyhedra represent, respectively, silicates and seven-fold coordinated calcium polyhedra). (For interpretation of the references to the color in this figure legend, the reader is referred to the web version of this article.)

structural region common to all samples. The hydrogen bonds observed by Raman spectroscopy are intra-main layer, and no hydrogen bonding links the main layer with the interlayer region of the structure. This induces a weak cohesion in the C–S–H stacking and explains the lack of long-range order in the direction perpendicular to the main layer. By using the empirical Falk law [39,41], the two groups of OH symmetric stretching from C–S–H compounds are related to hydrogen bond lengths (oxygen hydrogen bond donor to oxygen hydrogen bond acceptor inter atomic distance) around 2.73 and 2.86 Å. A systematic listing of the O–O inter atomic distances in the C–S–H structure, using the Tobermorite M structural model [42], indicates seven O–O distances in the ranges 2.73 and 2.86 Å (O4–O20: 2.89, O8–O19: 2.75, O10–O15: 2.76, O11–O13: 2.74, O12–O13: 2.73, O15–O17: 2.76 and O15–O16: 2.77 Å). From these seven possibilities only one corresponds to an intra-main layer hydrogen bond: the O4–O20 bonding. The O8–O19 bonding would correspond to a hydrogen bond linking two adjacent main layers; such a hydrogen bond across the interlayer would be sample dependent and does not agree with experimental observations. The five other possibilities involve two oxygen atoms belonging to the same paired silicate tetrahedron. These five possibilities are not acceptable, except in the case of a missing paired silicate tetrahedron which can lead to the creation of a hydrogen bond between the bridging silicate tetrahedron and the closed calcium oxide layer (represented by dashed black bonds in Fig. 5c). The compatible intra-main layer hydrogen bond links the seven apical oxygen atom of main layer calcium cation (those that are not bonded to a bridging silicate tetrahedron) to the oxygen atoms shared by two paired silicate tetrahedra (represented by full black bonds in Fig. 5c). The involvement of oxygen atoms linked to the sevenfold coordinated calcium in the hydrogen bond network is already well known in the case of AFm phases [28,29,38,43–45], in which hydrogen bonds are located across the interlayer region and participate strongly to the cohesion of the AFm stacking structure. The absence of hydrogen bonding across the interlayer region of C–S–H explains the described OD (order-disorder) character of the tobermorite structure due to a weak stacking energy of such a layered structure [46,47].

^{1}H MAS NMR spectroscopy: Single pulse ^{1}H MAS NMR presents the advantage to allow quantitative measurements, the area of the spectrum being directly related to the amount of ^{1}H nuclei. However, NMR line widths are dictated largely by dipolar homonuclear interaction, the magnitude of which is large (the dipolar constant is proportional to $\gamma^2_{(^1H)}/r^3$, where $\gamma_{(^1H)}$ and r are the magnetogyric ratio and the proton–proton distance, respectively) but may be modulated by molecular motion. Proton homonuclear dipolar coupling may be partially removed by MAS technique. One of the main observations is here the presence of two types of line width. Indeed ^{1}H MAS NMR spectra show close similarities regardless of both C–S–H and C–A–S–H series (Fig. 6a and b, Table 4): a broad band centered around 4.5 ppm, representing about 98% of the total ^{1}H population and some sharp resonances well defined in spite of their relative by low intensities. The signal of adsorbed water may be hidden by the broad response of hydrogen bond network. The former protons should be attributed to a hydrogen bond network as previously evidenced by Raman spectroscopy. Such protons encounter strong homonuclear dipolar broadening. Line position of the main signal agrees with previous work [48]; the line is here slightly high-field shifted. ^{1}H isotropic chemical shift if oxygen-bound hydrogen is known to depend linearly on the O–H···O distance as follows:

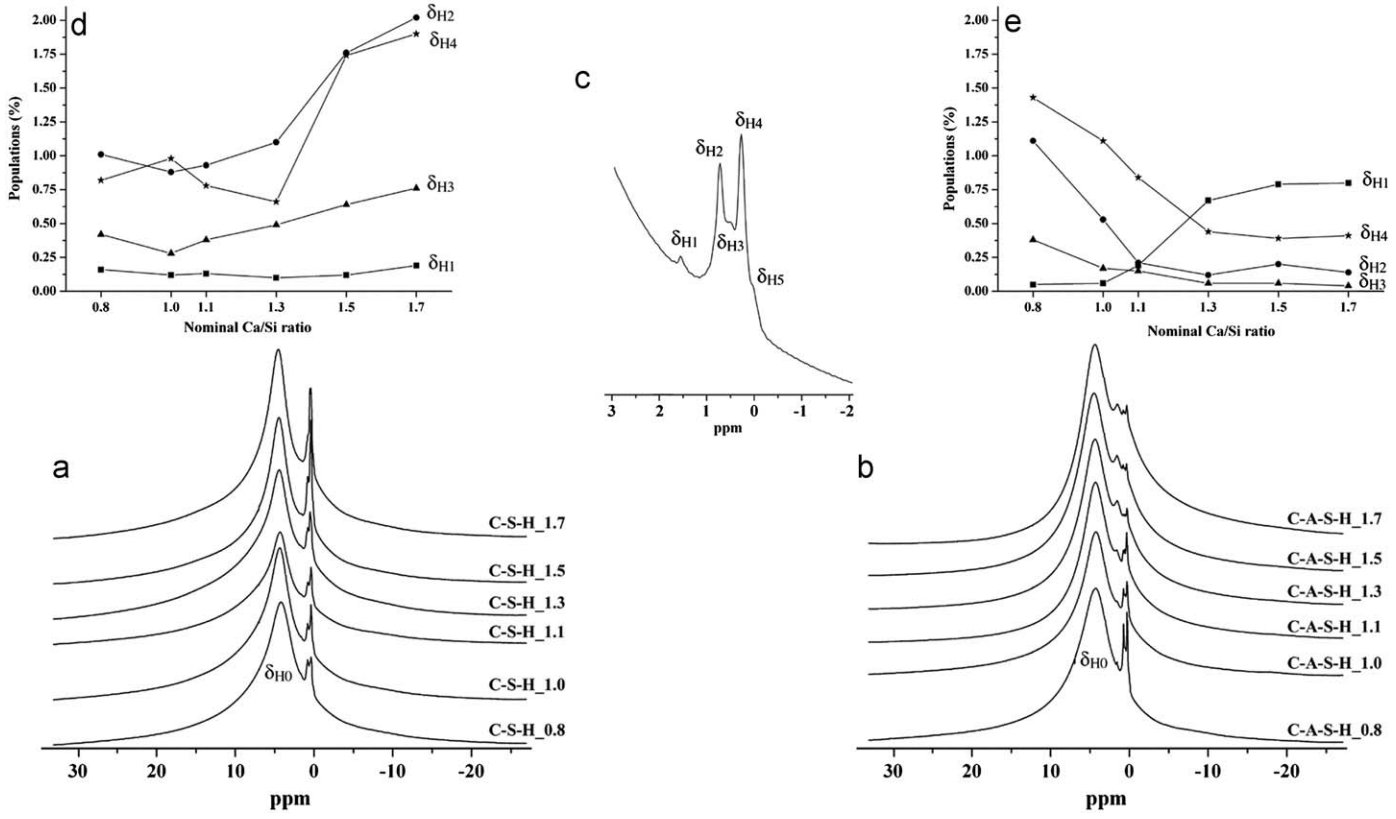

Fig. 6. ^{1}H MAS NMR spectra from samples belonging to (a) the C–S–H series and (b) the C–A–S–H series, with (c) detail showing the five sharp signals for sample C–S–A–H_0.8. Results of the profile fitting (normalized at 100% of hydrogen atoms) of the four main sharp components δ_{H1}, δ_{H2}, δ_{H3} and δ_{H4} are showing for (d) the C–S–H series and (e) the C–A–S–H series.

Table 4
Results of the profile fitting analyses in six components (δ_{H0}–δ_{H5}) of the ^{1}H MAS NMR spectra from the C–S–H and the C–A–S–H series.

Samples	δ_{H0}			δ_{H1}		δ_{H2}		δ_{H3}		δ_{H4}		δ_{H5}	
	ppm	FWHM[a] (kHz)	Pop. (%)[b]	ppm	Pop. (%)[b]	ppm	Pop. (%)[b]	ppm	Pop. (%)[b]	ppm	Pop. (%)[b]	ppm	Pop. (%)[b]
C–S–H_0.8	4.3	1.65	97.5	1.5	0.2	0.8	1.0	0.5	0.4	0.3	0.8	0.0	0.1
C–S–H_1.0	4.5	1.63	97.6	1.5	0.1	0.8	0.9	0.5	0.3	0.3	1.0	0.0	0.1
C–S–H_1.1	4.5	1.61	97.6	1.5	0.1	0.7	0.9	0.4	0.4	0.3	0.8	0.0	0.2
C–S–H_1.3	4.6	1.65	97.4	1.5	0.1	0.8	1.1	0.5	0.5	0.3	0.7	0.0	0.2
C–S–H_1.5	4.5	1.50	95.4	1.5	0.1	0.8	1.8	0.5	0.6	0.3	1.7	0.1	0.4
C–S–H_1.7	4.6	1.49	94.9	1.4	0.2	0.8	2.0	0.5	0.8	0.3	1.9	0.0	0.2
C–A–S–H_0.8	4.5	1.63	96.8	1.4	0.1	0.8	1.1	0.6	0.4	0.3	1.4	0.0	0.2
C–A–S–H_1.0	4.3	1.61	98.1	1.5	0.1	0.8	0.5	0.6	0.2	0.3	1.1	–	–
C–A–S–H_1.1	4.2	1.59	98.6	1.4	0.2	0.8	0.2	0.6	0.2	0.3	0.8	–	–
C–A–S–H_1.3	4.2	1.63	98.7	1.5	0.7	0.8	0.1	0.6	0.1	0.3	0.4	–	–
C–A–S–H_1.5	4.3	1.71	98.6	1.5	0.8	0.8	0.1	0.6	0.1	0.3	0.4	–	–
C–A–S–H_1.7	4.3	1.86	98.6	1.5	0.8	0.8	0.1	0.6	0.1	0.3	0.4	–	–

[a] Full width at half maximum.
[b] Relative populations of the six different signals obtained by profile fitting of the ^{1}H NMR spectra (normalized at 100% of hydrogen atoms).

δ_{iso}=79.05–0.255 $d_{(O–H\cdots O)}$, with δ_{iso} in ppm and $d_{(O–H\cdots O)}$ in pm [49]. An average $d_{(O–H\cdots O)}$ distance of 2.92 Å is then estimated. Additionally it is interesting to note that the full width at half maximum (FWHM) is almost constant for the C–S–H series, and of about 1.6 kHz, while it is increasing for the high Ca/(Si+Al) ratios for C–A–S–H series up to 1.9 kHz for C–A–S–H_1.7. Probably this difference may arise from the presence of quadrupolar ^{27}Al nuclei in a close vicinity of protons. Therefore such an additional and growing broadening in the C–A–S–H series must originate from the interlayer domain where heteronuclear dipolar coupling between ^{1}H and ^{27}Al[VI] takes place.

Table 4 gathers results of the profile fitting of the six components (δ_{H0} for the broad main component, and δ_{H1} to δ_{H5} for the five sharp components) and Fig. 6c provides in detail the isotropic chemical shifts corresponding to the sharp components. It appears that δ_{H5} component is preferentially observed in samples from the C–S–H series. Nevertheless their relative intensities are function to the Ca/Si ratio, and their variations are different between both C–S–H and C–A–S–H series (see Fig. 6d and e). The populations of the sharp components are increasing (respectively, decreasing) in the C–S–H series (respectively, C–A–S–H series) with the Ca/Si ratio. The δ_{H1} component only increases with the Ca/Si ratio in the C–A–S–H series, while it stays quite inexistent (with a population $<0.2\%$) in the C–S–H series whatever the Ca/Si ratio. The interpretation of such sharp ^{1}H NMR signals is not trivial, but $<2\%$ of the total population of hydrogen atoms is concerned. The probable explanation is that the very narrow liquid-like (or inclusion-like) peaks with FWHM in the range of 50 Hz are due to protons presenting a rapid tumbling or mobile on their dynamic exchange site and consequently experiencing very weak dipolar coupling (either homo- or hetero-nuclear) only. Finally, it is important to note that such a narrow line shape must occur from mobile ^{1}H nuclei relatively isolated from each other, and thus not from free water molecule. Rather than ^{1}H nuclei coming from adsorption of water on small domain, we surmise that they form pendant hydroxyl function.

4. Conclusion

Both NMR and Raman results give evidence for an effective structural continuity in C–S–H, C–A–S–H and C–N–A–S–H series. A previous study on long-range order investigated by Rietveld refinements on powder X-Ray diffraction patterns has shown the ability of a unique structural model (a 'tobermorite M defect' model) to describe the structure of C–S–H whatever the Ca/Si ratio. The insertion of aluminum during the synthesis of C–S–H systematically leads to a constant increase in the basal spacing of about 2 Å whatever the Ca/Si ratio (between 0.8 and 1.7). ^{27}Al MAS NMR spectroscopy indicates that the main part of aluminum atoms is four-fold coordinated at low Ca/Si, and is progressively replaced by six-fold coordinated aluminum atoms when increasing Ca/Si. Al[VI] becomes the main aluminates environment for high Ca/Si values. Long-range order results combined with local environment investigations give evidence of the location the six-fold coordinated aluminates readily into the interlayer region of the C–S–H (i.e. the C–A–S–H) structure. Previous works have shown a great affinity between C–S–H phase and an Al[VI] containing compound [23] as AFm phase [6,50]. It appears from present results, that this AFm-type entity should be directly inserted into the C–S–H compound in order to explain the 2 Å basal spacing increase observed in the presence of aluminum (a surface compound, whatever the affinity, will never involve such a basal spacing increase). For the same reason, Al[VI] should be connected to interlayer calcium cations, and not substituted to them, to involve this 2 Å basal spacing increase leading to the so-called AFm-type layer formed between the C–S–H main layers in C–A–S–H compounds. Sodium atoms intercalated into the C–S–H structure has a stabilizing feature to the formation of this AFm-type entity. Study of the hydrogen bond network has shown the existence of intra-main layer hydrogen bonding, and not of hydrogen bonding across the inter layer region. Such a hydrogen bond network leads to the apparent low crystallinity of C–S–H (actually small coherent domain size of crystalline phase), and the OD character of the tobermorite structure [46,47], due to a weak cohesion in the stacking sequence of this layered compound.

References

[1] H.F.W. Taylor, in: Cement Chemistry, second ed., Thomas Telford Publishing, New York, 1997.
[2] D.L. Rayment, A.J. Majumdar, Cem. Concr. Res. 12 (1982) 753–764.
[3] D.L. Rayment, Cem. Concr. Res. 12 (1982) 133–140.
[4] S.A. Rodger, G.W. Groves, J. Am. Ceram. Soc. 72 (1989) 1037–1039.
[5] I.G. Richardson, G.W. Groves, Cem. Concr. Res. 23 (1993) 131–138.
[6] I.G. Richardson, Cem. Concr. Res. 29 (1999) 1131–1147.
[7] C.A. Love, I.G. Richardson, A.R. Brough, Cem. Concr. Res. 37 (2007) 109–117.
[8] J. Skibsted, C. Hall, Cem. Concr. Res. 38 (2008) 205–225.
[9] H.F.W. Taylor, Chem. Soc. 33 (1953) 163–171.
[10] S.A. Greenberg, T.N. Chang, J. Phys. Chem. 69 (1965) 182–188.
[11] S.A. Greenberg, T.N. Chang, J. Phys. Chem. 69 (1965) 553–561.

[12] M. Grutzeck, A. Benesi, B. Fanning, J. Am. Ceram. Soc. 72 (1989) 665–668.
[13] Y. Okada, H. Ishida, T. Mitsuda, J. Am. Ceram. Soc. 77 (1994) 765–768.
[14] X.C. Cong, R.J. Kirkpatrick, Adv. Cem. Res. 7 (1995) 103–111.
[15] I. Klur, B. Pollet, J. Virlet, A. Nonat, in: A.-R. Grimmer, H. Zanni, P. Sozzani (Eds.), Nuclear Magnetic Resonance Spectroscopy of Cement Based Materials, Springer, Berlin, 1998.
[16] A. Nonat, X. Lecoq, in: A.-R. Grimmer, H. Zanni, P. Sozzani (Eds.), Nuclear Magnetic Resonance Spectroscopy of Cement Based Materials, Springer, Berlin, 1998.
[17] F. Brunet, Ph. Bertani, Th. Charpentier, A. Nonat, J. Virlet, J. Phys. Chem. B 108 (2004) 15494–15502.
[18] M.D. Andersen, H.J. Jakobsen, J. Skibsted, Inorg. Chem. 42 (2003) 2280–2287.
[19] I.G. Richardson, A.R. Brough, R. Brydson, G.W. Groves, C.M. Dobson, J. Am. Ceram. Soc. 76 (1993) 2285–2288.
[20] M.D. Andersen, H.J. Jakobsen, J. Skibsted, Cem. Concr. Res. 34 (2004) 857–868.
[21] P. Faucon, A. Delagrave, J.-C. Petit, C. Richet, J.M. Marchand, H. Zanni, J. Phys. Chem. B 103 (1999) 7796–7802.
[22] G.K. Sun, J.F. Young, R.J. Kirkpatrick, Cem. Concr. Res. 36 (2006) 18–29.
[23] M.D. Andersen, H.J. Jakobsen, J. Skibsted, Cem. Concr. Res. 36 (2006) 3–17.
[24] X. Chen, Ph.D. Thesis, Université de Bourgogne, Dijon, 2007.
[25] G. Renaudin, J. Russias, F. Leroux, F. Frizon, C. Cau-dit-Coumes, J. Solid State Chem., in press, doi:10.1016/j.jssc.2009.09.026.
[26] P. Faucon, T. Charpentier, D. Bertrandie, A. Nonat, J. Virlet, J.-C. Petit, Inorg. Chem. 37 (1998) 3726–3733.
[27] P. Faucon, T. Charpentier, A. Nonat, J.-C. Petit, J. Am. Chem. Soc. 120 (1998) 12075–12082.
[28] M. François, G. Renaudin, O. Evrard, Acta Cryst. C 54 (1998) 1214–1217.
[29] G. Renaudin, M. François, O. Evrard, Cem. Concr. Res. 29 (1999) 63–69.
[30] J. Skibsted, E. Henderson, H.J. Jakobsen, Inorg. Chem. 32 (1993) 1013–1027.
[31] P. Pena, J.M. Rivas Mercury, A.H. De Aza, X. Turrillas, I. Sobrados, J. Sanz, J. Solid State Chem. 181 (2008) 1744–1752.
[32] H. Viallis, P. Faucon, J.-C. Petit, A. Nonat, J. Phys. Chem. B 103 (1999) 5212–5219.
[33] Y. Kim, R.J. Kirkpatrick, Geochim. Cosmochim. Acta 61 (1997) 5199–5208.
[34] B.L. Phillips, R.J. Kirkpatrick, G.L. Hovis, Phys. Chem. Min. 16 (1988) 262–275.
[35] R.J. Kirkpatrick, J.L. Yarger, P.F. McMillan, P. Yu, X. Cong, Adv. Cem. Bas. Mat. 5 (1997) 93–99.
[36] K. Garbev, P. Stemmermann, L. Black, C. Breen, J. Yarwood, B. Gasharova, J. Am. Ceram. Soc. 90 (2007) 900–907.
[37] L. Black, C. Breen, J. Yarwood, K. Garbev, P. Stemmermann, B. Gasharova, J. Am. Ceram. Soc. 90 (2007) 908–917.
[38] G. Renaudin, J.-P. Rapin, B. Humbert, M. François, Cem. Concr. Res. 30 (2000) 307–314.
[39] G. Renaudin, R. Segni, D. Mentel, J.-M. Nedelec, F. Leroux, C. Taviot-Gueho, J. Adv. Concr. Tech. 5 (2007) 299–312.
[40] G. Renaudin, A. Bertrand, M. Dubois, S. Gomes, P. Chevalier, A. Labrosse, J. Phys. Chem. Sol. 69 (2008) 1603–1614.
[41] M. Falk, in: W.A. Adams, G. Greer, J.E. Desnoyers (Eds.), Chemistry and Physics of Aqueous Gas Solution, Electrochemical Society, Princeton, 1975, p. 19.
[42] S.A. Hamid, Zeit. Krist. 154 (1981) 189–198.
[43] G. Renaudin, M. François, Acta Cryst. C 55 (1999) 835–838.
[44] G. Renaudin, F. Kubel, J.-P. Rivera, M. François, Cem. Concr. Res. 29 (1999) 1937–1942.
[45] G. Renaudin, J.-P. Rapin, E. Elkaim, M. François, Cem. Concr. Res. 34 (2004) 1845–1852.
[46] S. Merlino, E. Bonaccorsi, T. Armbruster, Am. Miner. 84 (1999) 1613–1621.
[47] S. Merlino, E. Bonaccorsi, T. Armbruster, Eur. J. Miner. 12 (2000) 411–429.
[48] F. Méducin, B. Bresson, N. Lequeux, M.-N. de Noirfontaine, H. Zanni, Cem. Concr. Res. 37 (2007) 631–638.
[49] J.P. Yesinowski, H. Eckert, G.R. Rossman, J. Am. Chem. Soc. 110 (1988) 1367–1375.
[50] F. Bank, J. Schneider, M.A. Cincotto, H. Panepucci, J. Am. Ceram. Soc. 86 (2003) 1712–1719.